Journal of Catalysis **183,** 251–266 (1999)
Article ID jcat.1999.2399, available online at http://www.idealibrary.com on IDEAL®

# Molecular Structural and Morphological Characterization of Polymer-Supported Mo(VI) Alkene Epoxidation Catalysts[1]

S. Leinonen,* D. C. Sherrington,*,[2] A. Sneddon,* D. McLoughlin,† J. Corker,‡ C. Canevali,§ F. Morazzoni,§ J. Reedijk,‖ and S. B. D. Spratt#

*Department of Pure and Applied Chemistry, University of Strathclyde, 295 Cathedral Street, Glasgow G1 1XL, United Kingdom; †Department of Bioscience, University of Strathclyde, Royal College Building, 204 George Street, Glasgow G1 1XW, United Kingdom; ‡Department of Chemistry, University of Southampton, Southampton SO9 5NH, United Kingdom; §Department of Materials Science, University of Milan, Milan, Italy; ‖Leiden Institute of Chemistry, Gorlaeus Laboratories, Leiden University, Leiden, The Netherlands; and #Johnston Matthey Technology Centre, Reading, United Kingdom

Received September 17, 1998; revised December 18, 1998; accepted December 21, 1998

**Heterogeneous alkene epoxidation catalysts prepared by immobilization of species derived from $MoO_2(acac)_2$ on two polymers, a polystyrene *N*-hydroxypropyl aminomethylpyridine resin and a polybenzimidazole resin, are known to behave differently. The two catalyst species have now been characterized extensively in terms of both the molecular structure of the Mo(VI) centers and the resin morphologies, and significant differences have been demonstrated in both aspects. Molecular structural characterization has involved elemental analysis and FTIR, electronic, and X-ray photoelectron spectroscopies, together with EXAFS analysis and associated modeling. Morphological studies have employed high-resolution transmission electron microscopy with Mo mapping, $N_2$ sorption, and Hg intrusion porosimetry and solvent imbibition measurements. The differences observed account for the observed variation in catalytic behavior, and these structural and morphological differences are discussed in detail.** 

## INTRODUCTION

Over the last few years a range of highly active and selective polymer-supported Mo(VI) alkene epoxidation catalysts have been developed in the laboratory of one of the present authors. In each case the polymer-bound catalyst is used with t-butylhydroperoxide (TBHP) as the mono-oxygen source. The earliest examples employed polystyrene- and polymethacrylate-based resins to which specific ligand structures, e.g., aminomethylpyridine, were attached (1, 2), but later species have involved highly thermo-oxidatively stable resins, such as polybenzimidazole (PBI) (3, 4) and polyimides (5), as the support. In the case of the polybenzimidazole resin no separate ligand was introduced onto the resin matrix; instead, the benzimidazole residues of the backbone appear to act as the sites for coordination of the Mo(VI) centers. The PBI · Mo and other polymer imidazole-containing catalysts also differ from the polystyrene- and polymethacrylate-bound chelating ligand Mo complex catalysts, in that the latter have to be pretreated to form active catalysts by oxidation with *tert.*-butyl hydroperoxide (TBHP) prior to use as alkene epoxidation catalysts. In the absence of this pretreatment this group of polymer-based catalysts can display long induction periods before becoming active and selective catalysts (1, 4). In contrast, in the liquid-phase epoxidation of propene (3) PBI · Mo requires no pretreatment and is a highly active, selective, stable, and long-lived catalyst as made.

Why these differences arise has so far not been clear, and indeed a detailed knowledge of the molecular structure of the catalytic species, and of the morphology of the polymer support, has been largely absent. In the present paper we report on a collaborative effort that has been made to try to answer some of these questions, and although we are still short of a definitive model, the picture is now far clearer. In the course of preparing this manuscript a seminal paper appeared on the structural analysis of alumina-supported Mo-based alkene epoxidation catalysts to which reference is made later (6).

## EXPERIMENTAL

### *Polymer Catalysts*

Two samples of polymer-supported Mo catalysts were prepared essentially as reported in our earlier papers (2, 3). The first employed a poly(styrene-divinylbenzene) resin carrying an *N*-(2-hydroxypropyl)-2-aminomethylpyridine ligand, PSHPAMP (Scheme 1). This was kindly supplied by the Dow Chemical Company as development resin XFS43084 (7). The second employed a polybenzimidazole

[1] This paper is dedicated to our young colleague Dr. Judith Corker, who died tragically in early 1998.

[2] To whom correspondence should be addressed. Fax: 0141 548 4246. E-mail: M.P.A.Smith@Strath.ac.uk.



0021-9517/99 $30.00

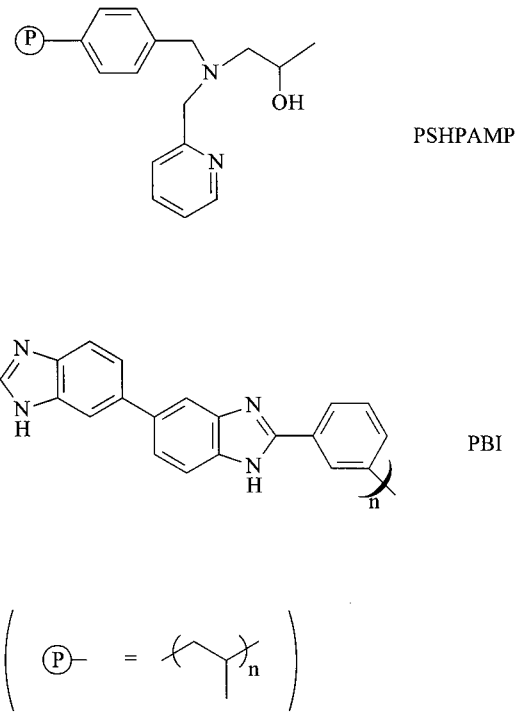


**SCHEME 1.** Polymer resin structures.

resin, PBI (Scheme 1). Originally we described our own synthesis of this (8) but the present sample was kindly supplied by the Hoechst–Celanese Company (9). Both resins were rather uniform high-quality spherical particulates. PSHPAMP had a particle diameter ~300–1000 $\mu$m, whereas the PBI beads were ~250–500 $\mu$m in diameter.

Each resin was purified by washing with 0.2 M NaOH for 24 h and deionized water until the washings were neutral. Each was then extracted with acetone in a Soxhlet and dried under vacuum at 40°C. Both samples of beads were beige in color. The elemental microanalytical data and nominal ligand content are given in Table 1.

**TABLE 1**

**Elemental Compositions of Resin and Resin Mo Catalysts**

| Resin/catalyst | Microanalytical data[a] (%) C | H | N | Ligand content (mmol g$^{-1}$) | Mo content[b] (mmol g$^{-1}$) | Nominal metal/ligand ratio |
|---|---|---|---|---|---|---|
| PBI | 70.3 | 4.9 | 15.7 | 5.6 | — | — |
| PBI · Mo | 50.8 | 3.0 | 11.6 | 4.15 | 2.1 | 1/2 |
| PSHPAMP | 78.4 | 7.75 | 7.4 | 2.65 | — | — |
| PSHPAMP · Mo | 55.3 | 5.5 | 5.25 | 1.9 | 2.0 | 1/1 |

[a] Determined using a Perkin–Elmer Series II analyzer.

[b] Sample dry-ashed with $KNO_3$/concentrated $HNO_3$ at 420°C; dissolved residue assayed using atomic absorption spectrophotometry (Philips PU9100X). See Ref. (11) for details.

Mo was loaded onto each resin by refluxing each sample with an excess of $MoO_2(acac)_2$ (Aldrich). The beads were allowed to cool and were collected by filtration. Following superficial washing in the filter each sample was exhaustively extracted in a Soxhlet, after which the solvent emerging from the thimble was colorless. Finally, the beads were vacuum dried at 40°C. Details of the experimental conditions used are listed in Table 2, and the corresponding analytical data on the Mo-loaded samples, PBI · Mo and PSHPAMP · Mo, are given in Table 1.

The PSHPAMP · Mo and PBI · Mo samples were each divided into two fractions. One fraction of each was designated "as made" and the other was activated by treatment with TBHP (Aldrich) as follows: PSHPAMP · Mo or PBI · Mo (1.0 g) was added to dry 1,2-dichloroethane (Aldrich distilled from $CaH_2$, 340 ml) and anhydrous TBHP in toluene [3.6 M, 3 ml, see Refs. (1, 10) for methodology]. The mixture was refluxed overnight and the beads collected by suction filtration. Dichloroethane and acetone were used respectively to wash the beads before vacuum drying (40°C). Both samples changed color slightly: PSHPAMP · Mo from dark to light beige, and PBI · Mo from light to darker green. These two fractions were designated "activated."

*Fourier Transform Infrared Analysis (FTIR)*

Resin samples were ground to a fine powder then made up into KBr disks in the normal way. Spectra were recorded on a Nicolet Impact 400D (Fig. 1).

*Electronic Spectra*

Resins were analyzed as produced using a standard holder with quartz windows. MgO was employed as a reference. UV–visible spectra were recorded on a Perkin–Elmer 330 spectrophotometer using the diffuse reflectance technique.

*X-Ray Photoelectron Spectroscopy (XPS)*

Each sample was dried under vacuum at 50°C for 10 h and then held on the sample stub using two-sided adhesive tape. X-ray photoelectron spectra were recorded on an M-Probe instrument (SSI-Fisons). The source was monochromatic Al$K\alpha$ radiation (1486.6 eV). The pressure in the analysis chamber was $5 \times 10^{-7}$ Pa. A spot size of 200 × 750 mm and a pass energy of 25 eV, with a resolution of 0.74 eV, were used. The energy scale was calibrated with reference to the $4f_{7/2}$ level of a freshly evaporated gold sample, taken as 84.00 eV with reference to the $2p_{3/2}$ level of copper at 932.47 ± 0.10 eV and the 3*s* level of copper at 122.39 ± 0.15 eV. The binding energy data of the carbon 1*s* region were used as an internal reference at 284.60 eV. The binding energy data for the resin samples and $MoO_2(acac)_2$ are summarized in Table 3.

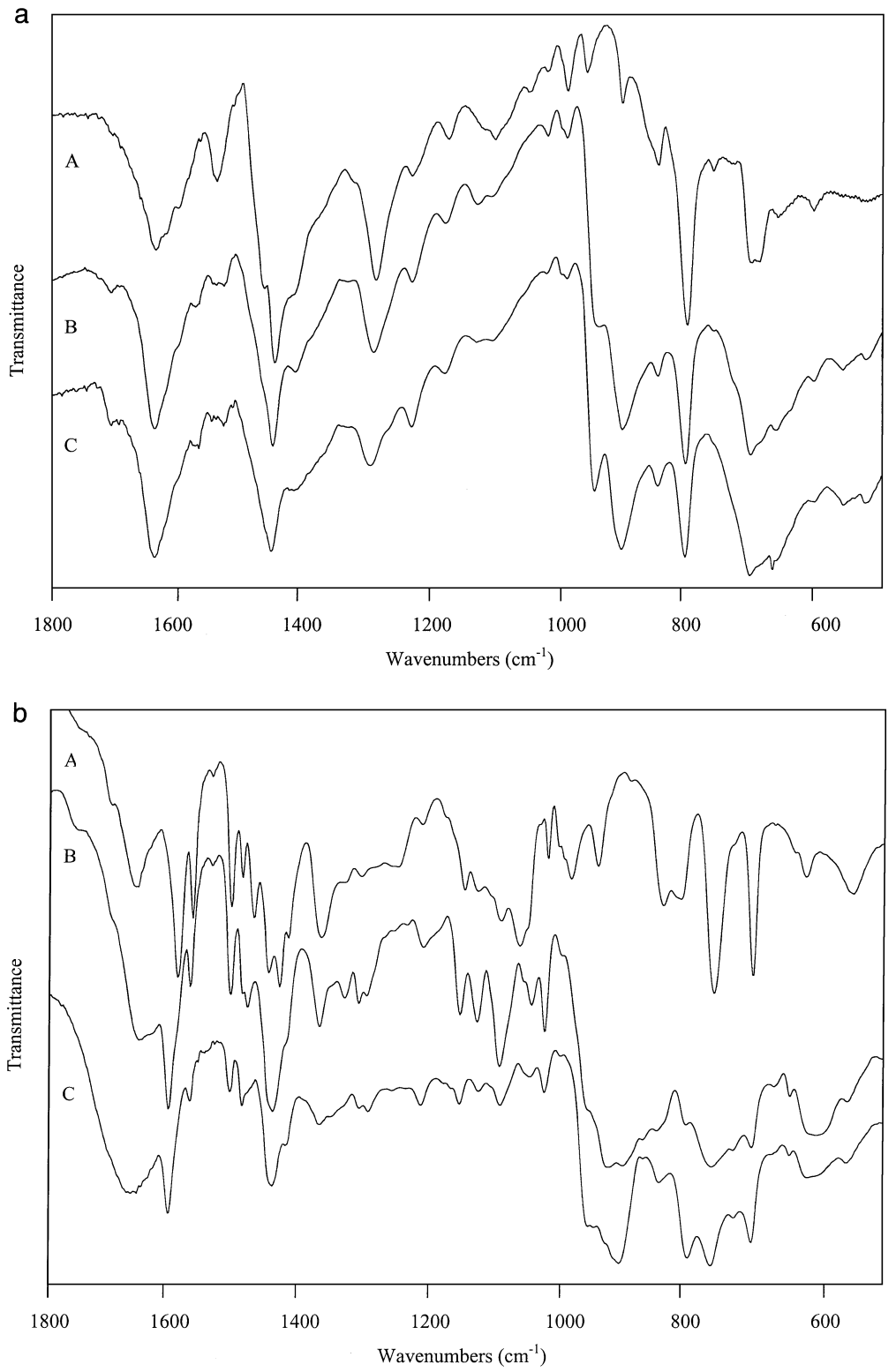


**FIG. 1.** (a) FTIR spectra of PSHPAMP (A) PSHPAMP · Mo "as made" (B), and PSHPAMP · Mo "activated" (C). (b) FTIR spectra of PBI (A), PBI · Mo "as made" (B), and PBI · Mo "activated" (C).

**TABLE 2**

**Experimental Details for Loading Resins with Mo**

| Resin (g, mmol ligand) | $MoO_2(acac)_2$ (g, mmol) | Solvent (ml) | Conditions | Extraction solvent, time | Product beads | |
|---|---|---|---|---|---|---|
| | | | | | Yield (g) | Color |
| PSHPAMP 3.47, 9.2 | 5.1, 15.6 | EtOH, 100 | 60°C, 3.5 h | Acetone, 3 days | 4.75 | Dark beige |
| PBI 4.0, 22.4 | 8.5, 26.0 | EtOH, 150 | 85°C, 3.5 h | Acetone, 3 days | 5.18 | Green |

*X-Ray Absorption Fine Structure (EXAFS) Analysis*

Each sample was ground to a fine powder and transferred to an aluminum sample holder with Kapton windows. Spectra were acquired at room temperature. X-ray absorption spectra for the Mo *K* edge were recorded on station 9.2 [Si(220) order-sorting monochromator] of the Synchrotron Radiation Source at the Daresbury Laboratory, United Kingdom, operating at 2 GeV and an average current of 180 mA. All the data were required in transmission mode.

The analysis of the EXAFS data was carried out in two stages. First, background-subtracted EXAFS data were obtained using the program PAXAS (12). The preedge subtraction used a second- or third-order polynomial, and the postedge background absorption was subtracted by fitting this region with coupled polynomials of order 7 or 8. This yielded the corresponding EXAFS spectra, i.e., the interference function $\chi(k)$, versus the photoelectron wave vector, $k$ (not reproduced here), together with the corresponding Fourier-transformed data plotted as amplitude versus $r$ (Å) (Fig. 2). Spherical wave curve-fitting analyses, by least-squares refinement of non-Fourier-filtered EXAFS, were then executed using the program EXCURV92 available on the xrsserv1 computer at the Daresbury Laboratory. In fitting the data a model is produced stepwise by adding one shell at a time, and statistical tests are used to assess the significance of each shell. Models are proposed based simply on plausible atomic constitutions. The results of this fitting exercise also appear in Fig. 2.

**TABLE 3**

**XPS-Derived Binding Energy Data for Polymer Resin Mo Catalysts and $MoO_2(acac)_2$**

| Sample | Center | Binding energy (eV) Mo $3d_{5/2}$ | Mo $3d_{3/2}$ |
|---|---|---|---|
| $MoO_2(acac)_2$ | | 232.91 | 236.05 |
| PSHPAMP · Mo "as made" | A | 232.45 | 235.55 |
| | B | 233.91 | 237.01 |
| PSHPAMP · Mo "activated" | A | 232.50 | 235.62 |
| PBI · Mo "as made" | A | 232.60 | 235.80 |
| | B | 233.62 | 236.89 |
| PBI · Mo "activated" | A | 232.67 | 235.77 |

*Transmission Electron Microscopy (TEM)*

Bead samples were prepared for sectioning by embedding with Taab resin [Taab resin (25 ml), dodecenylsuccinic anhydride (20 ml), methyl nadic anhydride (5 ml), benzyldimethylamine (0.5 ml)]. Beads were first infiltrated with resin for 48 h with four changes of resin charge. A small sample of these beads was placed into an embedding capsule and fresh resin added. The sample was polymerized at 70°C for 48 h. The resin block was removed from the capsule and 5-$\mu$m sections were cut using an LKB Pyramatone and mounted on glass slides. The blocks were further trimmed to the area of interest; then EM sections were cut between 80 and 90 nm using an LKB ultratome. These were mounted onto 300-mesh 3-mm copper grids.

Initially each sample was examined on an AEI EM6B microscope at 50 kV and low resolution (×230). Subsequently the same sections were examined on a Philips EM400T microscope operating at 20, 40, and 100 kV with a $C_2$ aperture of 50 $\mu$m and an analytical takeoff angle at +15° in micro- and nanoprobe modes. Brightfield images of PSHPAMP · Mo "as made" and "activated" were essentially identical and the latter (×25,000 and ×115,000) are shown in Fig. 3. Likewise the images of PBI · Mo "as made" and "activated" were very similar and the latter (×25,000 and ×115,000) are shown in Fig. 4. In addition, Mo$K\alpha$, X-ray elemental mapping was performed on the two PBI · Mo samples, and the image obtained for PBI · Mo "activated" together with the corresponding backscattered image is shown in Fig. 5. Unfortunately extensive beam damage to the PSHPAMP · Mo samples precluded any mapping work.

*Porosity Measurements*

$N_2$ sorption porosimetry was performed on a Micromeritics ASAP 2010 instrument. The surface area of each resin catalyst was calculated from data acquired in the relative pressure ($P/P_0$) range ~0.06–0.20 using BET theory (13), and the cumulative pore volumes and average pore radii

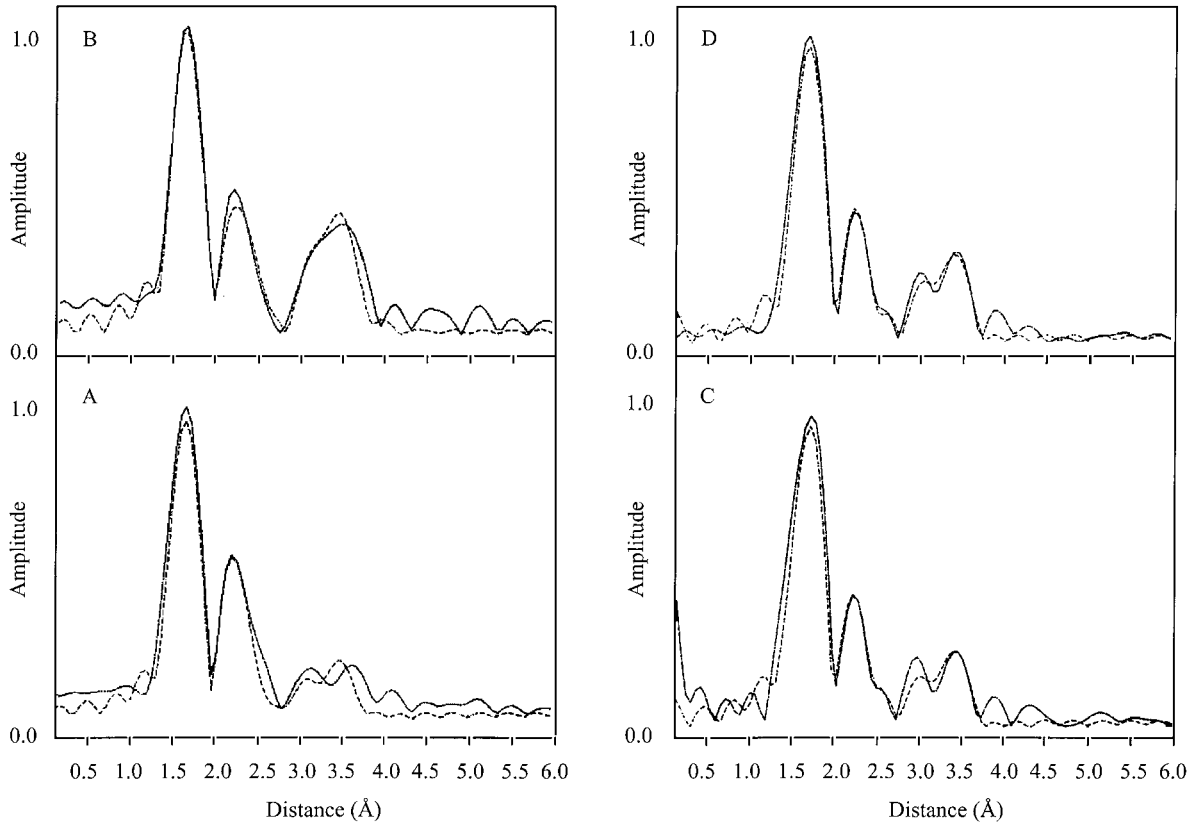


**FIG. 2.** Fourier transform EXAFS spectra of PSHPAMP · Mo "as made" (A) PSHPAMP · Mo "activated" (B), PBI · Mo "as made" (C), and PBI · Mo "activated" (D). Solid lines, experimental data; dotted lines, best theoretical fit.

were computed from the full adsorption isotherms using BJH theory (14). The data obtained are summarized in Table 4. Hg intrusion porosimetry was also carried out using a Micromeritics Autopore II and dedicated software. Corresponding data on surface area, intrusion volume, and average pore radius for all four resins are given in Table 4. Each resin catalyst was prepared for analysis as described earlier under Polymer Catalysts.

*Solvent Uptake*

The amount of toluene imbibed by the nonloaded resins and the corresponding Mo-containing resins "as made"

**TABLE 4**

**$N_2$ Sorption and Hg Intrusion Porosimetry Data for Polymer Resin Mo Catalysts**

| Porosity parameter | Resin catalyst | | | |
|---|---|---|---|---|
| | PHPAMP · Mo "as made" | PHPAMP · Mo "activated" | PBI · Mo "as made" | PBI · Mo "activated" |
| Hg intrusion | | | | |
| Surface area ($m^2\ g^{-1}$) | 72 | 61 | 122 | 111 |
| Pore volume (ml $g^{-1}$) | 0.40 | 0.36 | 1.40 | 1.53 |
| Average pore radius ($\mu$m) | 0.011 | 0.012 | 0.028 | 0.023 |
| $N_2$ sorption | | | | |
| Surface area ($m^2\ g^{-1}$)[a] | 35 | 31 | 8 | 18 |
| Cumulative pore volume (ml $g^{-1}$)[b] | 0.21 | 0.29 | 0.04 | 0.10 |
| Average pore radius ($\mu$m)[b] | 0.012 | 0.018 | 0.010 | 0.011 |

[a] BET calculations.
[b] From BJH theory.

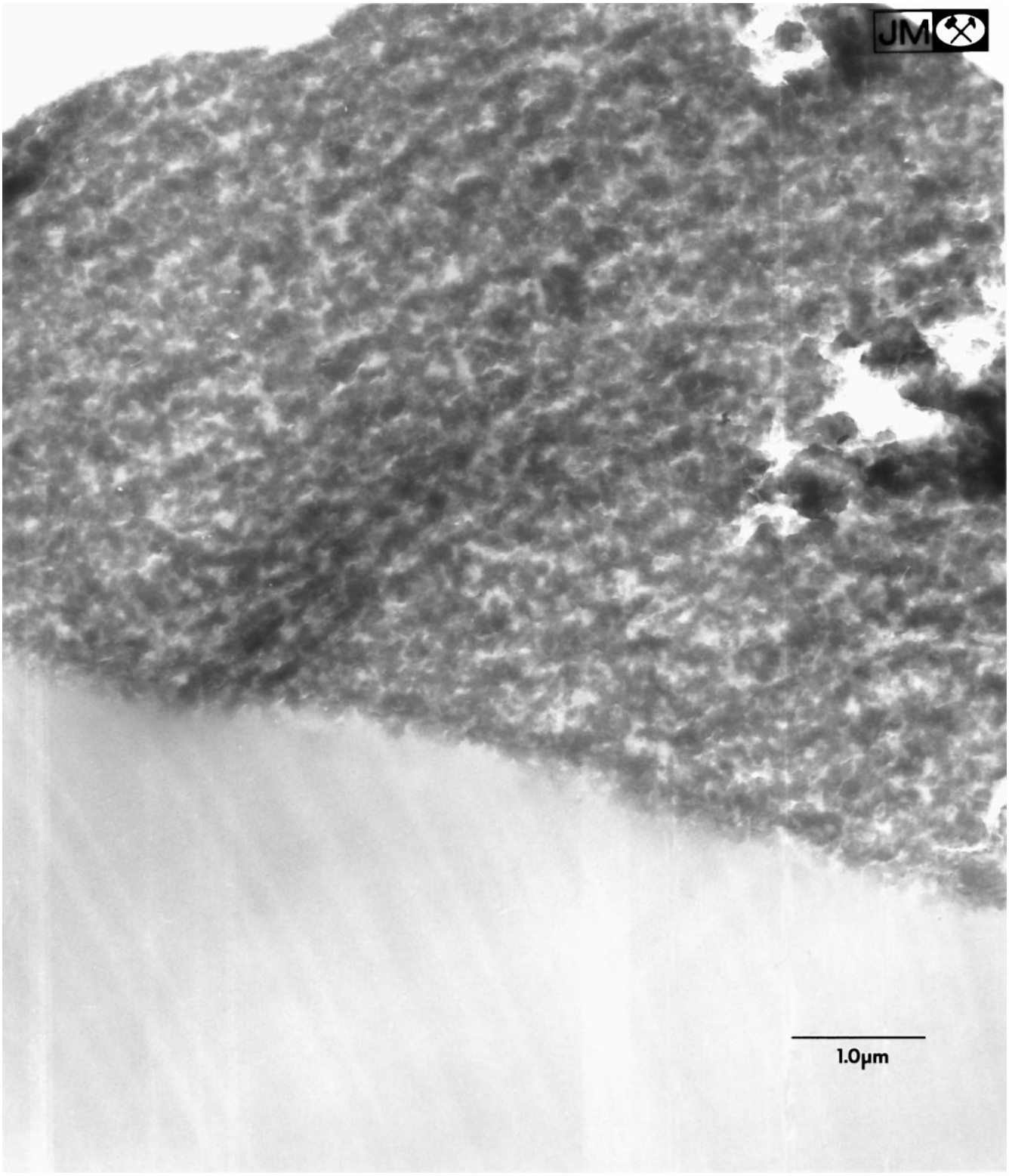


**FIG. 3.** High-resolution TEM images of section of PSHPAMP · Mo "activated" (×25,000 and ×115,000).

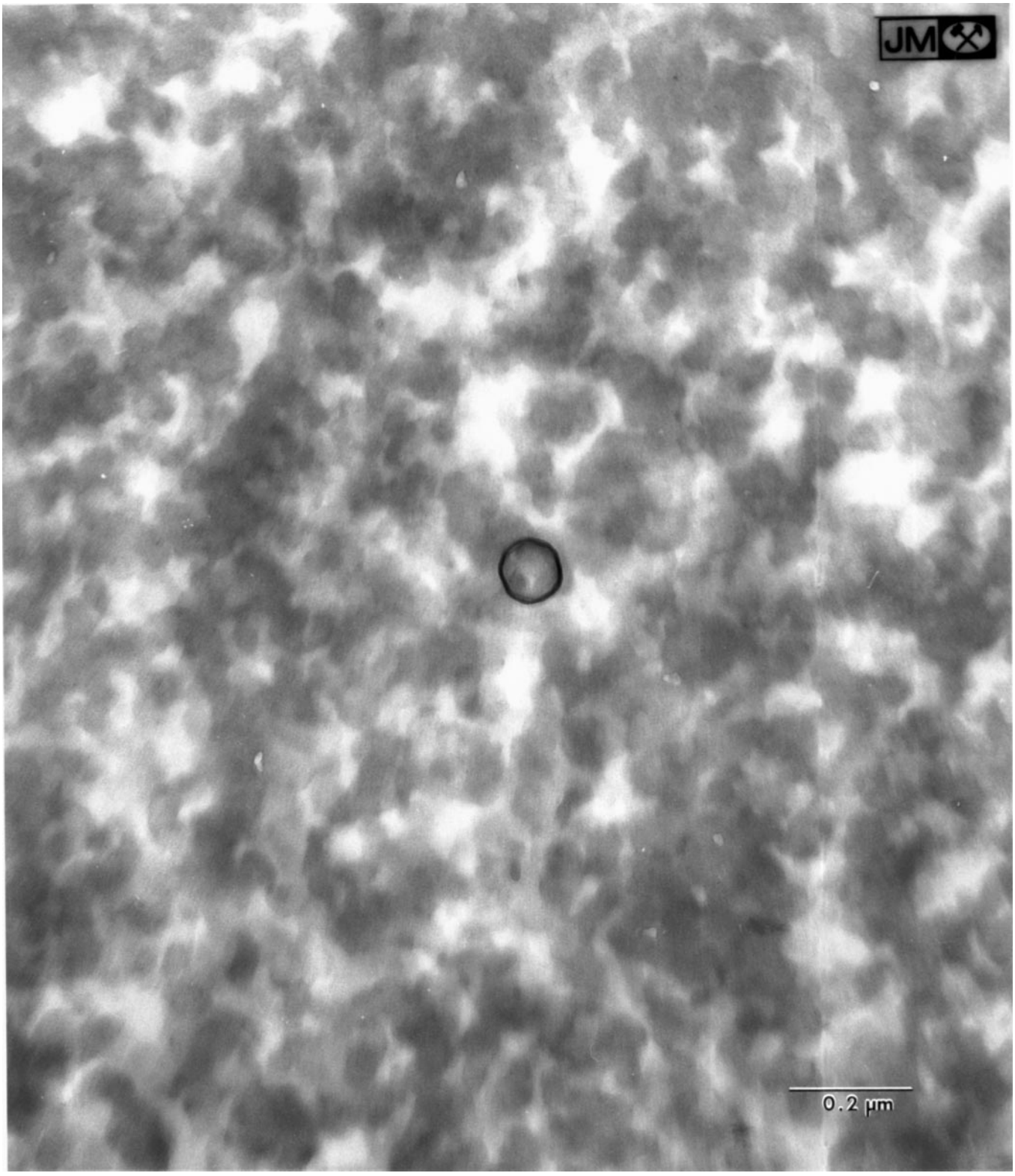


**FIG. 3**—*Continued*

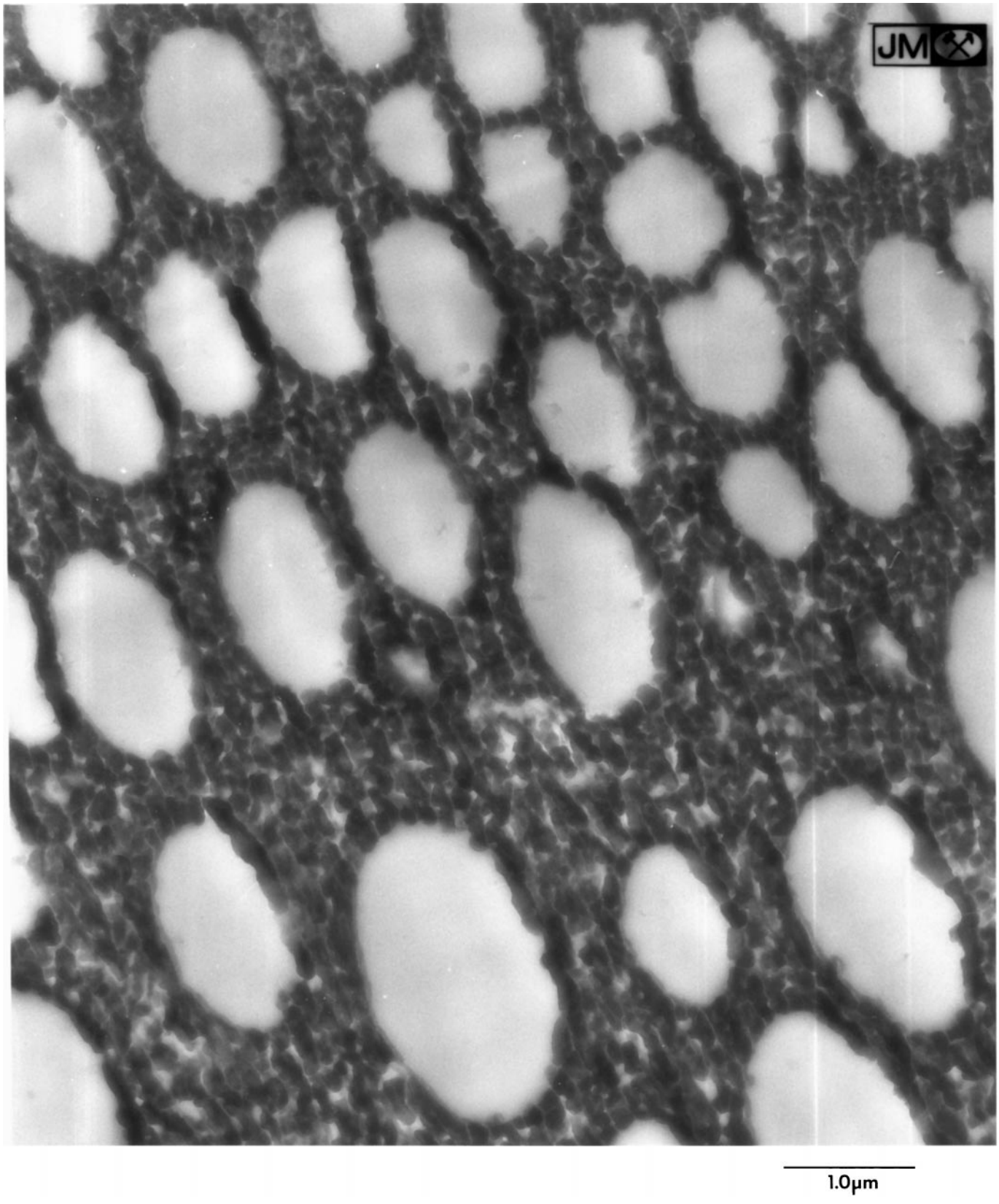


**FIG. 4.** High-resolution TEM images of Section of PBI · Mo "activated" (×25,000 and ×115,000).

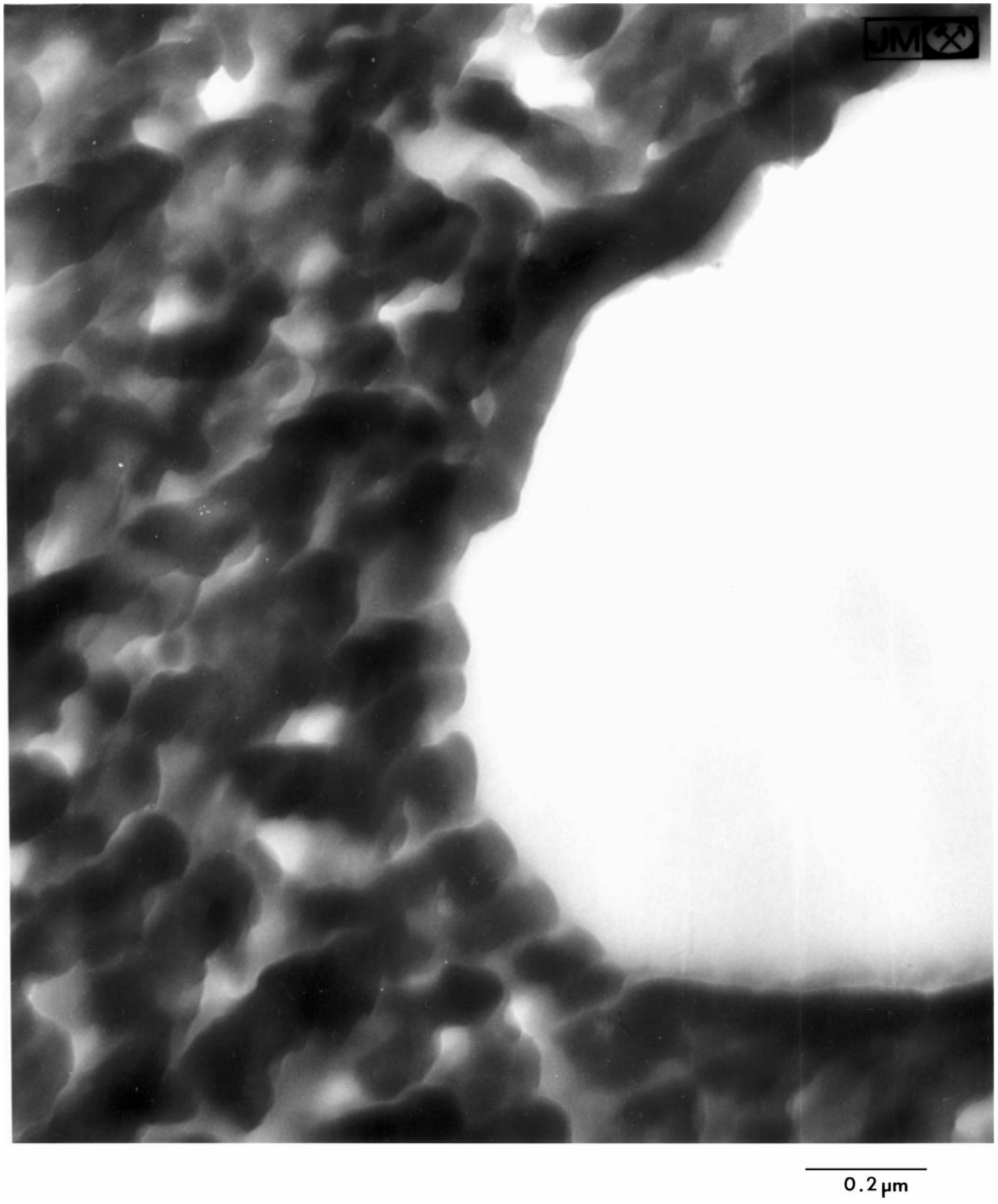


**FIG. 4**—*Continued*

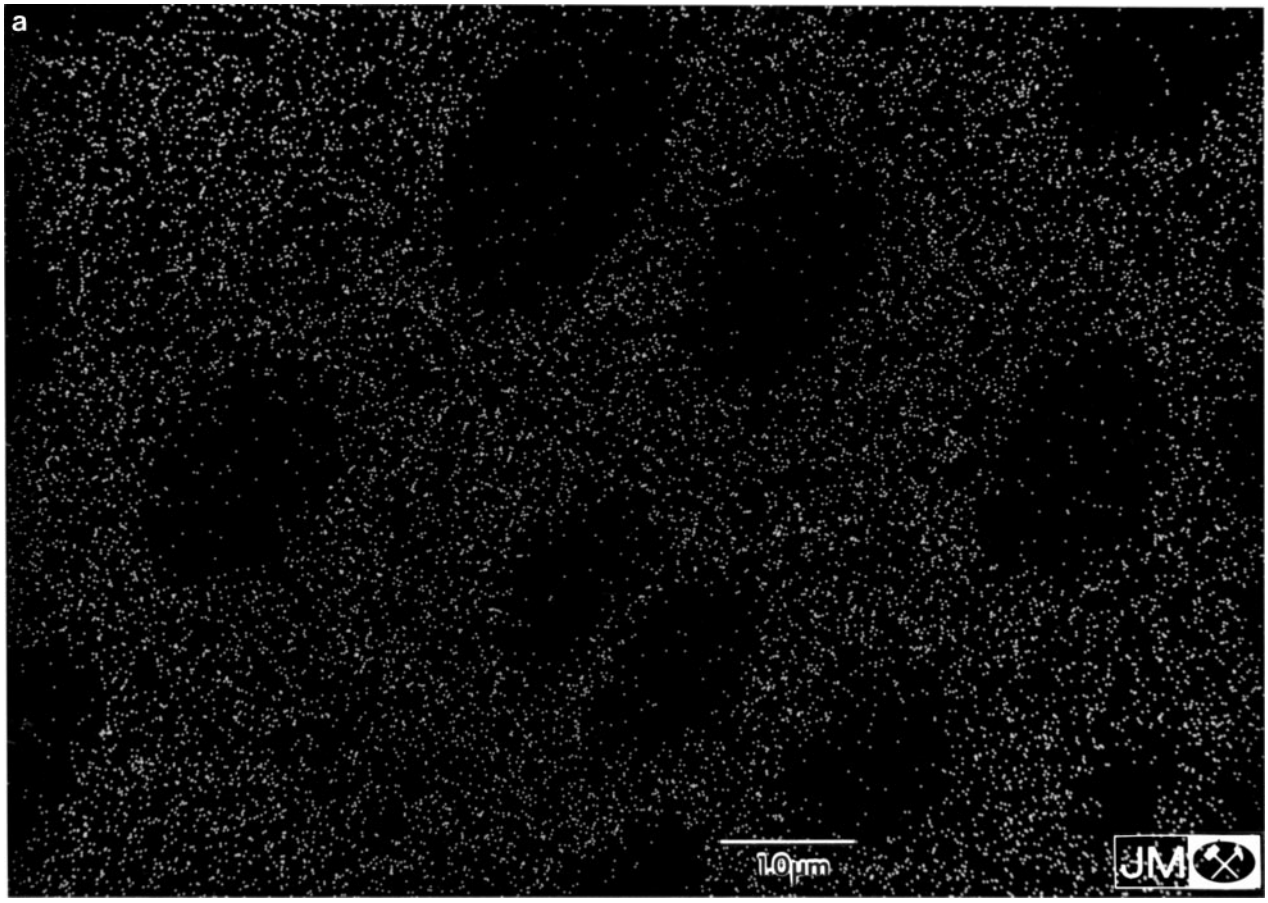


**FIG. 5.** (a) Mo$K\alpha$ X-ray elemental map of section of PBI · Mo "activated" (×18,000). (b) Corresponding backscattered image of (a) complementing the same field of view (×18,000).

was determined gravimetrically using a sample centrifugation method (15). The values for PBI, PBI · Mo "as made," PSHPAMP, and PSHPAMP · Mo "as made" are 1.84, 1.22, 0.50, and 0.28 g toluene $g^{-1}$ resin, respectively.

## RESULTS AND DISCUSSION

### *Composition and Molecular Structure of Polymer-Supported Mo Catalysts*

*Elemental composition and FTIR spectral analysis.* The elemental compositions of the PBI and PSHPAMP resins and the "as made" Mo-loaded analogues are given in Table 1. The ligand content of the precursor resins (estimated from N%) and the corresponding ligand and Mo contents of the loaded species are of the same order as previously found in earlier work (3, 4) and, indeed, represent good reproducibility in the synthesis of these catalysts. The nominal metal/ligand ratios of ~1/2 and ~1/1 for PBI · Mo and PSHPAMP · Mo superficially suggest that each Mo center is associated with two imidazole ligands and one hydroxypropylaminomethylpyridine ligand, respectively, in these catalysts. Since activation of the latter with TBHP causes only minor loss of Mo [typically ~1% (2)] the metal/ligand ratios in the activated analogues must be almost identical. Bearing in mind the extended backbone nature of these organic supports and the random nature of the interpenetration of individual polymer chains, highly efficient use of all ligands in coordinating to Mo centers seems unlikely. Consequently, placing too much emphasis on the possible structural interpretation of these ratios is not justified. Perhaps of most importance is the observation that the Mo centers become bound, they are tightly held, and their low leaching in catalytic application is a common feature.

The FTIR spectra (Fig. 1) of the precursor resins, the Mo-loaded species, and the activated species show the same trends. On loading PSHPAMP with Mo, bands appear centered around ~905 and ~950 $cm^{-1}$ characteristic of Mo=O symmetric and antisymmetric stretches, and there is a broadening of an existing PSHPAMP band at ~705 $cm^{-1}$ to encompass the absorption at ~720 $cm^{-1}$, most likely associated with stretching of Mo–O–Mo bridges (16). Likewise there is broadening at ~610 $cm^{-1}$ which may also be associated with Mo–O–Mo groups (17) (Fig. 1a). Small changes

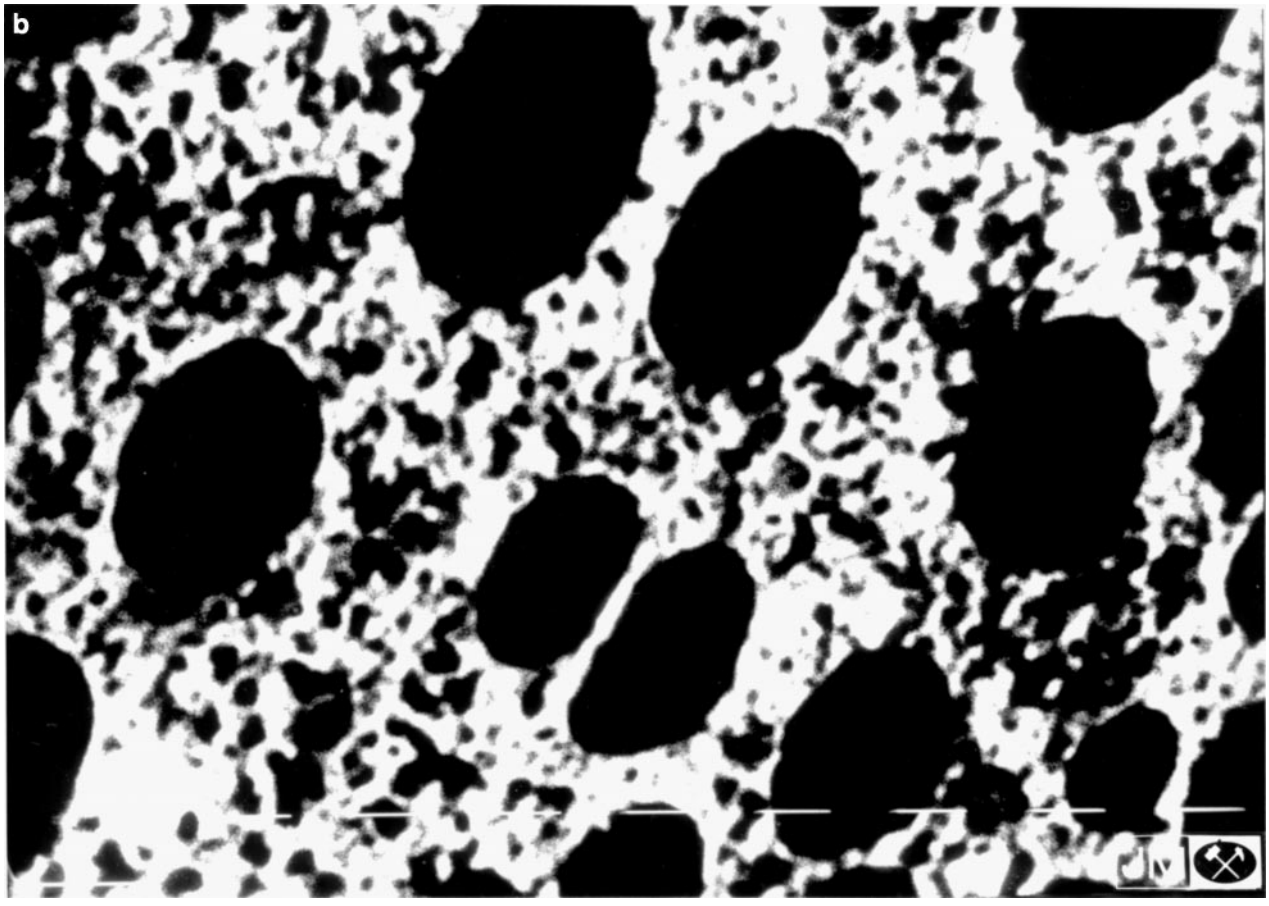


**FIG. 5**—*Continued*

also occur in bands in the region 1300–1600 $cm^{-1}$ but these are not sufficiently clear-cut to show definitively the presence of $acac^-$ ligands. Activation of PSHPAMP · Mo with TBHP causes little additional change though perhaps with some extra broadening in the band around ~700 $cm^{-1}$. Similarly, loading of the PBI resin with Mo produces additional broad absorptions at ~900–950 $cm^{-1}$ and centered at ~700 $cm^{-1}$ (Fig. 1b). Again these can be assigned to Mo=O and Mo–O–Mo bond vibrations. Changes in the region around 1300–1600 $cm^{-1}$ are only relative and minor, and again cannot be used diagnostically in terms of the presence or absence of the acac ligand. Treatment of the sample with TBHP causes minor sharpening of the bands around 900–950 and 700 $cm^{-1}$ but no major additions or deletions. Overall, therefore, the FTIR spectra confirm the incorporation of Mo centers in both resins with the molecular structure involving both Mo=O and Mo–O–Mo features. These appear to change little on treatment with TBHP.

*EPR spectra, XPS analysis and electronic spectra.* Electron paramagnetic resonance spectra (not reported in detail here) were recorded at liquid $N_2$ temperature and these indicated that the level of Mo(V) present is always very low ($10^{-3}$–$10^{-4}$%). In $MoO_2(acac)_2$ as a control the level detected was ~$10^{-4}$%. This increases to ~$10^{-3}$% on loading Mo onto both resins, and falls back again with PBI · Mo when the resins are oxidized with TBHP. Both resins therefore have an electron donor effect initially, which seems to be lost on oxidation with TBHP in the case of PBI · Mo. The above effects, however, are very small and the overwhelming proportion of Mo centers are in the +VI oxidation state.

In the XPS analysis, again only Mo(VI) centers were detected, and the binding energy data obtained (Table 3) do show some interesting and consistent changes. $MoO_2(acac)_2$ as a control yields values for Mo $3d_{5/2}$ and Mo $3d_{3/2}$ of 232.91 and 236.05 eV, respectively. After loading onto both resins two new Mo(VI) centers have been detected, one with binding energy higher (B centers) than that seen for Mo in the control, and one with a slightly lower binding energy (A centers). The latter are probably associated with electron-donating polymer ligand groups. The A centers in PBI · Mo represent ~60% of the total Mo, and in PSHPAMP · Mo the corresponding figure is ~50%. On activation with TBHP all the B centers are lost from both resin catalysts, and since there is no significant metal loss during this treatment it seems likely that all Mo centers are

converted into the A type. To some extent these results are difficult to reconcile with the EXAFS data that follow, but it is important to remember that the XPS technique probes specifically the surface of the sample and that the structures detected may not be representative of the "average" structures located in the internal bulk of the sample. Overall, therefore, the XPS data suggest that there is little difference between the two resin Mo catalysts and that treatment with TBHP converts all the Mo centers into more structurally homogeneous species, at least in terms of the surface sites.

The electronic spectra (not reported in detail here) of all four Mo-loaded resins were rather similar. However, in this case there is some evidence that the PSHPAMP · Mo "as made" sample differs somewhat from the PBI · Mo "as made" sample. In particular, the broad UV–visible band remains more intense above a wavelength of ~560 nm where there is a clear shoulder. On activation structural changes appear to take place in this sample with the corresponding UV–visible absorption band becoming very similar to that of PBI · Mo "as made" and "activated" samples. This spectral similarity in the "activated" samples and difference in the "as made" samples run contrary to the later EXAFS data and cannot be reconciled to date.

*EXAFS analysis and structural modeling.* In some ways the EXAFS data are perhaps the most informative in indicating the molecular structure of the Mo centers in these supported species. However, it is vital to remember at the outset that where a structural diversity of species arises, the traditional approach to modeling the resultant EXAFS spectrum can give an indication only of the average structural environment, in this case, around the Mo centers.

With the PBI · Mo "as made" the FT EXAFS spectrum (Fig. 2C) shows many of the features reported by Imamura *et al.* (6) for Mo(VI) species immobilized on aluminas. The best theoretical structural fit obtained using reasonably plausible guesses suggests an average Mo environment shown as **3** in Fig. 6, i.e., two Mo=O bonds of 1.67 Å, two Mo–O bonds of 2.27 Å, two Mo–N bonds of 2.41 Å, and an Mo–Mo interaction at 3.22 Å. Again the latter agrees well with the recent literature (6). The two N atoms most likely arise from two different imidazole residues. The changes in the EXAFS spectrum of the PBI · Mo "activated" sample (Fig. 2D) are so small that the same best-fit structure applies. Bearing in mind that the EXAFS experiment probes the bulk of a sample, it does seem that the binding energy changes seen in the XPS data and the associated loss of one of two initially present Mo(VI) centers are indeed mainly surface effects and are probably not relevant in terms of the catalytic behavior. For the PBI · Mo species the situation seems reasonably simple in that interaction of $MoO_2(acac)_2$ with the imidazole residues on the polymer leads primarily to dinuclear structures of the form **4** (Fig. 7), with concomitant aerobic oxidation possibly playing a role.

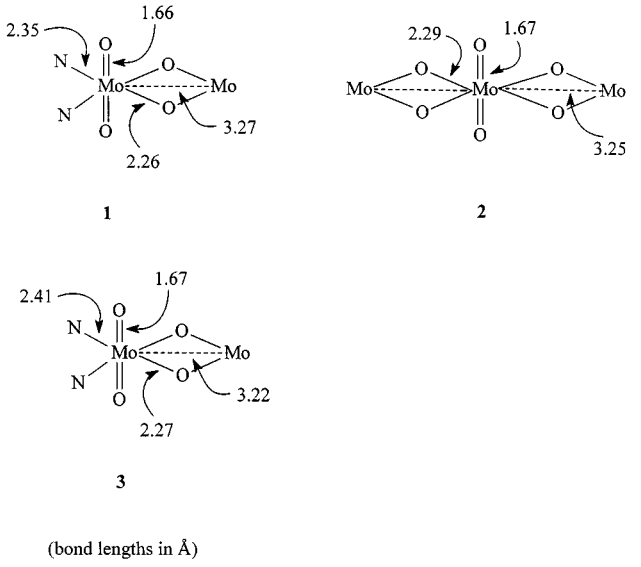


**FIG. 6.** Best-fit structures for "Average" Mo centers in PSHPAMP · Mo "as made (**1**); PSHPAMP · Mo "activated" (**2**); PBI · Mo "as made" (**3**); and PBI · Mo "activated" (**3**).

This dinuclear species represents the resting structure of the catalyst. In the presence of TBHP, **4** is most likely transformed to the active monometallic catalytic species **5** as proposed by Sharpless *et al.* (18) and Mimoun (19), but on removal of the oxidant the resting structure reforms. The PBI · Mo "activated" sample as analyzed is therefore in the resting state (**4**). The only major issue remaining concerns the nature of the N–Mo bond and the relationship of the two N atoms. Stereochemical considerations exclude that these two N centers would reside on the same imidazole ring, and the most likely structure involves donation from two N atoms on two different imidazole residues. It remains perfectly plausible for one imidazole group to bridge two Mo centers and, hence, to be involved potentially in the coordination sphere of two active sites. The relative $pK_a$ values of imidazole and acacH are such that displacement of $acac^-$ by the former could also involve an exchange of a proton. However, the presently available experimental data shed no light on this. Further sophistication of the EXAFS modeling is possible and there is some suggestion of an additional shell of C atoms around 3.2–3.6 Å from Mo. This seems very reasonable and is not inconsistent with the likely location of the C atoms in the imidazole ring. Overall, therefore, the structural picture seems a little different from that which we proposed earlier (4) and, in particular, the "as made" and resting structure of the PBI · Mo system appears to be a dinuclear species.

The situation with the PSHPAMP support seems to be somewhat more complex. The FT EXAFS spectrum for PSHPAMP · Mo "as made" (Fig. 2A) is rather similar to those of the PBI · Mo samples, and so not surprisingly the best theoretical fit structure for the "as made" sample, again

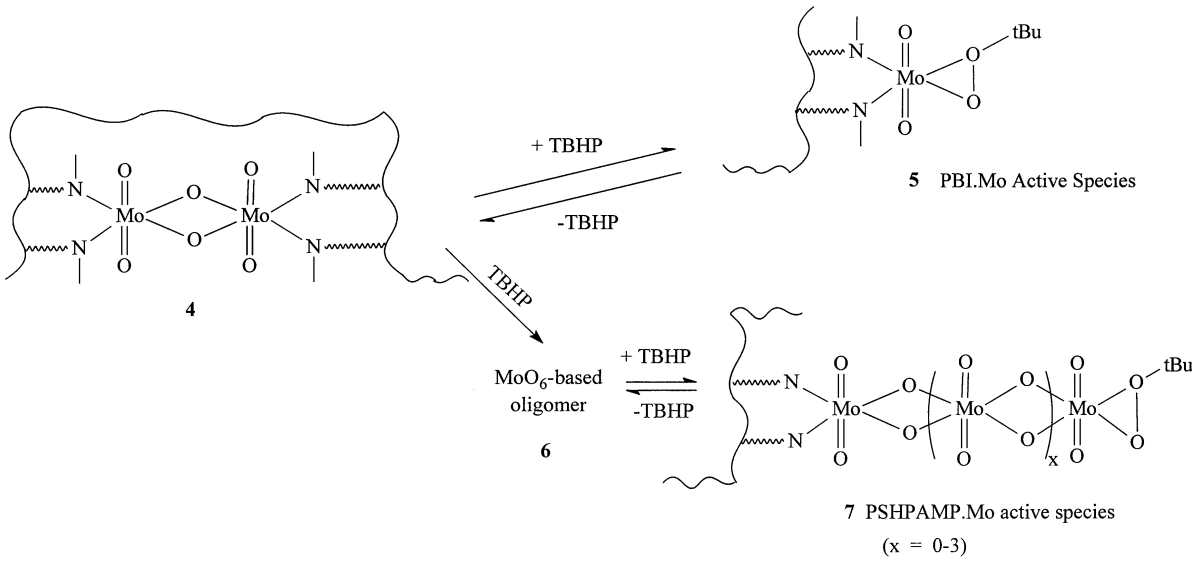


**FIG. 7.** Mostly likely structures for Mo complexes supported on PBI and PSHPAMP and the active catalytic centers formed from these.

using reasonably plausible structural guesses, suggests an average Mo environment, shown as **1** in Fig. 6, very similar to that found for PBI · Mo (**3**). With PSHPAMP · Mo the two N atoms most likely arise as a chelating pair from a single aminomethylpyridine residue. The dilemma that arises is why should this structure not transform rapidly on treatment with TBHP to form a catalytically active mononuclear species similar to that envisaged for PBI · Mo? Why also should this system give rise to an induction period in TBHP-driven alkene epoxidations? The situation becomes more complicated when the FT EXAFS spectrum (Fig. 2B) for the activated form of PSHPAMP · Mo is modeled. This generates the best-fit structure shown as **2** in Fig. 6. On average each Mo center has two Mo=O bonds of 1.67 Å, four Mo–O bonds of 2.29 Å, and two Mo interactions at 3.2 Å. The requirement for a relatively large increase in electron density at ~3–3.5 Å is seen even by visual inspection of the FT EXAFS curve (Fig. 2B) and can be met only by the presence on average of two additional Mo centers flanking each Mo center. Growth in the electron density of ~3–3.5 Å is again consistent with a picture of a move toward aggregated octahedrally coordinated Mo centers reported by Imamura *et al.* (6), and we concur with the latter group that the active Mo(VI) center is undoubtedly octahedrally coordinated.

Mo(VI) oxo chemistry in aqueous systems is dominated by the formation of $MoO_6$ octahedra and the very favorable formation of $[Mo_7O_{24}]^{6-}$ (20, p. 954). Oligomeric structures with $7 > Mo > 1$ are very rare. The situation in the absence of water is less certain but amine ligands generally give rise to structurally ill-defined complexes (20, p. 949), although there are exceptions (16). It does seem reasonable, therefore, that small oligomers of Mo(VI) octahedrally surrounded by six O atoms might form (**6**) (Fig. 7), although as will be shown later transmission electron microscopy suggests that these must be of limited size and certainly cannot be $MoO_3$ crystallites. In any event the structures generated are the basis of potent alkene epoxidation catalysts. Why though should such oligomeric structures form with the PSHPAMP support, but not with the PBI support, and, of course, why should the initially formed dinuclear species on PSHPAMP (≡**4**) (Fig. 7) not be immediately catalytically active as is the case with PBI? The answer to this may be in the different morphologies of the supports (see below) but one possibility on the molecular structural scale concerns the structure of the amine ligands. Whereas imidazole (ImH) residues may be able to protonate an $acac^-$ ligand while displacing this as neutral acacH, the $pK_a$ of aminomethylpyridine residues makes the analogous process less likely. The bonding of Mo(VI) centers to the soformed $Im^-$ residues may therefore be somewhat stronger than to the neutral aminomethylpyridine groups, despite the chelating nature of the latter. Bearing in mind also the known tendency for well-defined neutral amine Mo(VI) complexes *not* to form (20, p. 949), the PSHPAMP · Mo complex may readily undergo an oligomerization process, especially in the presence of an oxygen donor, e.g., TBHP, to generate octahedrally coordinated $MoO_6$ units (**6**) and an oligomeric reactive species such as **7** (Fig. 7). Presenting the argument somewhat differently, relatively stronger coordination by deprotonated and potentially bridging imidazole ligands may inhibit the tendency for oligomerization to occur. The observed induction period in alkene epoxidations using PSHPAMP · Mo may therefore arise from the competitive favorable oligomerization process, which once complete provides novel structures also capable of generating active catalytic centers (**7**) (Fig. 7). In the case of $MoO_3 \cdot H_2O$ immobilized via ion exchange of $MoO_4^{2-}$ onto Amberlite IR 120 resin (21) the similarly observed need for

activation of the polymeric catalyst was shown to be associated with the role of increasing the acidic character of the Mo(VI) species. A corollary of the argument developed in the present work is that once PSHPAMP · Mo is activated, i.e., the Mo is converted to its oligomeric state, the catalyst should remain active and, in particular, should not display an induction period in recycling experiments. In the case of propene as the substrate this is essentially true (3). However, with cyclohexene some level of induction is retained (1). Since loss of activity also occurs on recycling with some alkenes, evaluating the effects unambiguously is rather difficult. It does seem, however, that this molecular structural explanation for the induction period is not the whole story and suggests that the polymer support morphology may also play a role.

*Morphological Structures of Polymer-Supported Mo Catalysts*

*TEM studies.* The low-resolution TEM images (×230) (not reproduced here), despite some mechanical damage to the PSHPAMP · Mo samples, showed an immediate and remarkable superficial difference in the two supports. The PSHPAMP resin is reported as being prepared by a suspension vinyl polymerization process [see patents cited in Ref. (7)] and its visually opaque appearance suggests it to have been made in the presence of a porogen; i.e., the resin falls into the category of being "macroporous" as used by the ion-exchange resin business (22), and indeed our TEM analysis seems to confirm this. Unfortunately, even when carefully embedded in a proprietary medium this resin shattered on attempts to microtome it. However, it is clear that the PSHPAMP · Mo samples do not contain large voids or cells, unlike the PBI · Mo samples which have a well-developed network of these. PBI is made in a suspension polycondensation process and it is likely that phenol and water are expelled at very high temperature in the course of this (9), and that these volatiles are the likely source of the large voids or cells. Corresponding high-resolution (×25 K, and ×115 K) TEM images are shown in Figs. 3 and 4 where the morphological differences are very clear. There is no obvious difference between the PBI · Mo "as made" and "activated" (Fig. 4) samples and the large voids or cells (typically ∼1–2 $\mu$m in diameter) are seen clearly with a well-developed system of interconnecting pores. The latter appear to lie between a fused mass of discrete, rather uniform polymer globules each typically ∼0.1 $\mu$m in size with pores themselves of rather broad size distribution, but typically ∼0.05 $\mu$m in diameter. Nothing can be deduced regarding morphological features below this size. The images for PSHPAMP · Mo "as made" and "activated" (Fig. 3) are also very similar to each other. Neglecting the mechanical damage to the samples, there are no large cells as seen in the case of the PBI-based samples. There is, however, a porous texture, somewhat less developed than that of the PBI-based samples and possibly somewhat finer. Only at magnification 115,000 do clear breaks (pores?) in the sample cross sections become apparent. These images will be useful in the discussion of the $N_2$ sorption and Hg intrusion data below.

Another important feature in the high-resolution TEM (×115,000) images is the absence of any small areas of relatively high electron density that might be associated with large crystallites of $MoO_3$. If, for example, species of ∼1000 Å (0.1 $\mu$m) were present, then these would undoubtedly be visible as clear features in the electron micrographs. Evidence for the presence of Mo was provided only from the Mo$K\alpha$ X-ray elemental map of the section of PBI · Mo "activated" and the corresponding backscattered image (Fig. 5). These show a relatively uniform distribution of Mo throughout the sample. There is no evidence of Mo nucleation at the surface of the large cells, though it is tempting to say that, if anything, Mo species are localized around the pores interconnecting the large cells. The resolution available, however, means that it is not possible to be definitive about this. Unfortunately, the PSHPAMP-based samples suffered too much beam damage to allow backscattering and mapping data to be accumulated.

Overall, therefore, the TEM images show the PBI-based catalyst to have a much more open structure than the PSHPAMP-based analogue with large cells interconnected by a well-defined and extensive network of macropores (and perhaps mesopores).

*$N_2$ sorption and Hg intrusion porosimetry data.* The porosimetry data for the PSHPAMP · Mo "as made" and "activated" samples were essentially identical and are discussed together; likewise the corresponding data for the two PBI · Mo samples are discussed together. Considerable care is needed in comparing the data obtained from application of these two techniques, and not least it must be remembered that while $N_2$ sorption data can be interpreted productively in the pore size range ∼0.1–0.0003 $\mu$m, Hg intrusion data are in the pore size range ∼300–0.01 $\mu$m. Interestingly the valid overlap range is rather narrow. Overall porosity parameters, pore volume, surface area, etc., computed from experimental data, therefore not only are dependent on the models exploited in deriving the parameters, but also are limited by the data obtained in the respective valid pore size regimes. Any parameters computed from experimental data obtained outside these limits are likely to be erroneous (23). The parameters deduced in this instance are summarized in Table 4 and were computed from data secured in the valid ranges respectively.

The pore size distribution curves (not reproduced here) for the PSHPAMP-based samples derived from Hg intrusion data show a sharp peak at a radius of ∼0.02 $\mu$m and the calculated average pore radius is ∼0.012 $\mu$m. No other features appear in the data and the overall pore volume is ∼0.38 ml $g^{-1}$. The analogous curves for the PBI-based

samples show a similarly sharp peak at a radius of ~0.03 $\mu$m, but with a small shoulder on the higher side of each curve. The calculated average pore radius is ~0.025 $\mu$m and the pore volume ~1.45 ml $g^{-1}$. These values correlate remarkably well with the TEM images described earlier, with the PSHPAMP-based species having somewhat finer (smaller radius?) less well developed (smaller volume?) pores. Somewhat remarkably, however, the pore size distribution curves for the PBI-based species show no evidence of pores in the size range ~1–2 $\mu$m (which in principle should be readily detectable by Hg intrusion) corresponding to the clearly visible cells in the TEM images. This presumably arises because these cells can be accessed only via the network of 0.05-$\mu$m pores and insofar as the Hg intrusion experiment is concerned, the large cells can be filled only at the higher pressure required to penetrate the smaller 0.05-$\mu$m connecting pores. The pore volume for the PBI-based samples is also calculated on this assumption as well.

The $N_2$ adsorption/desorption isotherms (not reproduced here) are all very similar and show a very small initial uptake of gas at relative pressures $P/P_0 < 0.1$ followed by a fairly linear and shallow rise until $\sim P/P_0 \sim 0.8$ and culminate in a steep rise as $P/P_0$ approaches 1. The major difference between the PSHPAMP-based samples and the PBI-based samples is that the shallow rise reaches ~20 $cm^3$ $N_2$ $g^{-1}$ in the former samples, whereas in the latter it reaches only ~7.5 $cm^3$ $g^{-1}$. The final sorption with the PSHPAMP species is ~150 and ~50 $cm^3$ $g^{-1}$ for the PBI species. The computed parameters in Table 4 reflect these differences. All four curves show a minor hysteresis effect on the desorption cycle from $P/P_0 = 1$ down to $P/P_0 = 0.8$. Thereafter, hysteresis is negligible. In all cases the small adsorption at low $P/P_0$ (<0.1) indicates that the level of true microporosity (i.e., pores <20 Å) is rather limited. The pore size distribution curve calculated from the full isotherm using the BJH treatment (14) for the PSHPAMP-based resins shows a broad maximum at ~0.03–0.05 $\mu$m and it seems very likely that this feature corresponds to the maximum seen at ~0.02 $\mu$m in the Hg intrusion data. The other feature of these curves is a steady rise in the population of pores with a pore size ~0.003 $\mu$m downward and the experimental data accumulated are not adequate enough, nor is the BJH theory sufficiently valid, to place too much significance on the absolute values of pore size in this part of the distribution. (*Note*: The instrument employed is capable of being operated to yield very meaningful data in the micropore region; however, with the present samples of low microporosity this was viewed to be not worthwhile.) The corresponding pore size distribution curves for the PBI-based species surprisingly showed no significant maxima around pore sizes in the range 0.03–0.05 $\mu$m as was anticipated from the Hg intrusion data. It is just possible, however, that this feature falls outside the $N_2$ sorption range. Again, a low level of micropore presence is indicated as well, but could not be quantified with the data at hand.

*Porosity parameters.* The computed porosity parameters are listed in Table 4. Bearing in mind the enormous difference in experimental techniques, the limitation of each method, and the requirement to model both sets of data to yield parameters with a convenient physical significance, the agreement between the parameters for the PSHPAMP-based species obtained from the Hg intrusion and $N_2$ sorption experiments is very good. In contrast, considerable differences arise with the PBI-based species in the case of the surface area and pore volume parameters. These differences almost certainly arise from the presence of the large cells or voids in these species. As far as the $N_2$ sorption experiment is concerned, cells ~1–2 $\mu$m in diameter will simply not be detected and so the surface area of these, and particularly their pore volume, will not contribute to the parameters calculated from the $N_2$ sorption data. This, in particular, explains the apparently very low pore volume of ~0.04–0.1 ml $g^{-1}$ registered by this technique, with the figure of ~1.5 ml $g^{-1}$ from the Hg intrusion data probably being more realistic (see solvent imbibition below). In contrast, however, the surface area of ~110–120 $m^2$ $g^{-1}$ provided by the Hg intrusion data seems high, and again this is probably an artifact arising from the need to intrude Hg into the large cells via the much smaller connecting pores. The technique therefore counts all this intruded volume as being contained in pores of the connecting size and hence overestimates the surface area of pore walls. Since both PBI- and PSHPAMP-based species seem to have relatively low micropore components the TEM images and derived data suggest that the PBI-based species may have a somewhat lower surface area than the PSHPAMP-based samples, so that surface area parameters derived from the $N_2$ sorption data look more realistic.

Since these polymer-based catalysts are in practice used in contact with solvent (e.g., toluene), rather than in the dry state, it is important to remember that though extensive TEM and porosity data are an important guide, some flexibility in interpretation may well be necessary when correlating with catalytic activity. With the present materials the PBI-based species typically sorb ~1.5 ml toluene $g^{-1}$, and the PSHPAMP-based species, ~0.4 ml toluene $g^{-1}$. These values are remarkably close to those calculated from the Hg intrusion data, and suggest that the "dry" porosity parameters may not alter substantially in the toluene "wet" state.

### *Catalyst Activity, Structure, Morphology Correlation: Summary*

The major difference in behavior between the PBI · Mo and PSHPAMP · Mo species is that the former are very active catalysts in liquid-phase alkene epoxidation

without any preactivation by oxidation. In contrast, PSHPAMP · Mo catalysts show an induction period before also becoming active and the induction period can be eliminated by activation with oxidant in advance of use in catalysis. The various molecular structural characterization studies show that the Mo centers formed in PBI · Mo are largely dinuclear species with two Mo(VI) centers, each with two Mo=O groups and both linked by two oxo bridges. Each Mo center is also coordinated by two N donors from different imidazole ligands, $Im^-$. Activation of this catalyst and subsequent structural analysis yield a very similar molecular structure. It seems, therefore, that this is the resting state of the catalyst and rapid cleavage of the oxo bridges of the bimetallic species in the presence of TBHP generates the active monometallic catalyst (**5**) (Fig. 7) which readily reverts to the resting state (**4**). Evidence from XPS data for two different Mo(VI) centers in PBI · Mo "as made" and loss of one of these on activation seems to be restricted to resin surface sites only.

In the case of PSHPAMP · Mo "as made" molecular structural characterization points to the presence of species very similar to those found in PBI · Mo (i.e., **4**) (Fig. 7). On activation with TBHP, however, oligomerization of the Mo centers occurs with the formation probably of a range of structures with, on average, each Mo center being flanked by two others (**6**) (Fig. 7). Essentially all metal centers are Mo(VI) each with two Mo=O groups and pairs of centers linked by two oxo bridges. Terminal Mo centers are probably coordinated by chelating neutral aminomethylpyridine ligands. Favorable generation of these oligomers in competition to catalysis of epoxidation seems to contribute in part to the induction period observed. The actual catalytic species is likely to be formed by cleavage of flanking Mo centers by TBHP with the formation of terminal species (**7**) (Fig. 7). The resting state seems most likely to be the oligomers (**6**). There is no evidence of significant growth to form $MoO_3$ crystallites.

Since PSHPAMP · Mo "activated" can also display an induction period on reuse with some alkenes the above molecular structural picture is not the complete story. The morphological studies show the remarkable open porous structure of the PBI-based species centered on large cells ~1–2 $\mu$m in diameter and connected by a well-developed system of macropores ~0.05 $\mu$m in diameter. The overall pore volume is substantial (~1.5 ml $g^{-1}$) and the whole porous structure is rapidly accessed by liquid phases. In contrast, the PSHPAMP · Mo-based species are typical of "macroporous" polystyrene-based resins and have a much finer and tighter network of pores and a significantly smaller pore volume. Mass transfer limitations through the latter species seem likely to contribute to the observed induction period, and prolonged activation may not be necessary to achieve molecular structural changes at the Mo centers, but rather to provide and improve access.

## ACKNOWLEDGMENT

We acknowledge receipt of a research studentship for S.L. from The Neste Oy Foundation and resources from the EPSRC to complete the EXAFS. We thank Mr. G. A. van Albada, Leiden University, for recording the UV–vis–NIR diffuse reflectance spectra.

## REFERENCES

1. Sherrington, D. C., and Simpson, S., *J. Catal.* **131**, 115 (1991).
2. Sherrington, D. C., and Simpson, S., *React. Polym.* **19**, 13 (1993).
3. Miller, M. M., and Sherrington, D. C., *J. Chem. Soc. Perkin Trans. 2*, 2091 (1994).
4. Miller, M. M., and Sherrington, D. C., *J. Catal.* **152**, 368, 377 (1995).
5. Ahn, J. H., and Sherrington, D. C., *J. Chem. Soc. Chem. Commun.*, 643 (1996).
6. Imamura, S., Sasaki, H., Shono, M., and Kanai, H., *J. Catal.* **177**, 72 (1998).
7. Grinstead, R. R., *J. Met.*, 13 (1979).
8. Brock, T., and Sherrington, D. C., *Polymer* **33**, 1773 (1992).
9. Buckley, A., Stuetz, D. E., and Serad, G. A., *in* "Encyclopedia of Polymer Science and Engineering" (H. F. Mark, N. Bikales, C. G. Overberger, G. Menges, and J. I. Kroschwitz, Eds.), 2nd ed., Vol. 11, p. 572, Wiley, New York, 1998.
10. Sharpless, K. B., and Verhoeven, T. R., *Aldrichim. Acta* **12**, 63 (1979).
11. Olason, G., and Sherrington, D. C., *in* "Proceedings, 7th International Symposium on Macromolecular–Metal Complexes." *Macromol. Symp.* **131**, 127 (1998).
12. Binsted, N., "PAXAS Programme for the Analysis of X-ray Absorption Spectra." University of Southampton, Southampton, 1988.
13. Brunauer, S., Emmett, P. H., and Teller, E., *J. Am. Chem. Soc.* **60**, 309 (1938).
14. Barrett, E. P., Joyner, L. G., and Halenda, P. P., *J. Am. Chem. Soc.* **73**, 373 (1951).
15. Greig, J. A., and Sherrington, D. C., *Polymer* **19**, 163 (1978).
16. Mitchell, P. C. H., *Q. Rev.* **20**, 103 (1966).
17. Mortimer, R., Powell, J. G., Greenblatt, M., McCarroll, W. H., and Ramanujachary, K. V., *J. Chem. Soc. Faraday Trans.* **89**, 3603 (1993).
18. Sharpless, K. B., Townsend, J. M., and Williams, D. R., *J. Am. Chem. Soc.* **94**, 295 (1972).
19. Mimoun, H., *J. Mol. Catal.* **7**, 1 (1980).
20. Cotton, F. A., and Wilkinson, G., "Advanced Inorganic Chemistry," 3rd ed. Interscience, New York, 1972.
21. Morazzoni, F., Canevali, C., D'Aprile, F., Bianchi, C. L., Temptesti, E., Giuffré, L., and Airoldi, G., *J. Chem. Soc. Faraday Trans.* **91**, 3969 (1995).
22. Sherrington, D. C., *J. Chem. Soc. Chem. Commun.*, 2275 (1998).
23. Webb, P. A., and Orr, C., "Analytical Methods of Fine Particle Technology," Chap. 3, p. 53; Chap. 4, p. 155. Micromeritics Instrument Corp., Norcross, 1997.